THE JOURNAL OF PHYSICAL CHEMISTRY B

pubs.acs.org/JPCB Article

Oligo(L-glutamic acids) in Calcium Phosphate Precipitation: Mechanism of Delayed Phase Transformation

Putu Ustriyana, F. Marc Michel, Michael C. Wilson, Emma Harmon, Jiahui Chen, Tianbo Liu, and Nita Sahai*

Cite This: J. Phys. Chem. B 2020, 124, 6288–6298 Read Online

ACCESS | Metrics & More | Article Recommendations | Supporting Information

ABSTRACT: Proteins and their mimics that contain negatively charged sequences are important in natural and biomimetic mineralization. The mechanism by which these sequences affect calcium phosphate mineralization is not well understood. Here, peptides containing different numbers of repeat units of contiguous glutamic acid residues, oligo(L-glutamic acid)$_n$ (n = 3, 7, 8, 10), were investigated with regards to the mechanism in delaying the crystallization of amorphous calcium phosphate (ACP) while holding the amount of carboxylic acid groups in solution constant. Increasing peptide chain length increases the stability of ACP at a certain total amount of carboxylic acid groups in solution. This effect is shown to be due to stronger binding as well as binding to more calcium ions per peptide by the longer oligopeptides compared to the shorter ones. It is proposed that these associations delay the structural rearrangement of calcium ions and the dehydration of ACP, which are required for the crystallization of hydroxyapatite. The initial nucleation and the local structure of ACP, however, do not vary with chain length. This second part of a two-part series provides an improved mechanistic understanding of how organic additives, especially those with contiguous acidic amino acid sequences, modulate the kinetics of calcium phosphate precipitation and phase transformation.

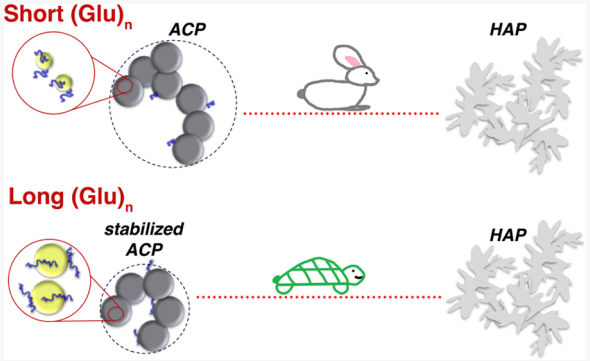

1. INTRODUCTION

Calcium phosphate is the main inorganic matrix of bones and teeth. In vivo, the biomineralization process is well controlled spatially and temporally to form different phases of calcium phosphates.[1] In vertebrate biomineralization, calcium phosphates are closely associated with the presence of numerous organic biomacromolecules including negatively charged proteins.[1] Previous research has focused on the effects of different proteins, namely osteopontin, dentin matrix protein 1, and bone sialoprotein, which possess a large number of acidic residues along their sequences or their mimics on the biomineralization process.[1−9] Small changes in the reaction conditions affect the formation of calcium phosphates in vitro.[10−12] The presence of these different additive molecules not only changes the course of the reaction but also affects the final results of the precipitation process.

The formation of crystalline calcium phosphate generally proceeds through the formation of a metastable amorphous calcium phosphate (ACP) precursor.[10,12−16] It has been proposed that the ACP consists of spherical clusters, known as Posner's clusters (PC, $Ca_9(PO_4)_6$)[17] that can aggregate to form larger particles.[18] The Ca/P ratio of the amorphous phase varies depending on the precipitation condition, such as pH and ion concentrations, with the ratio ranging from 1.18 to 2.50.[10] The ACP eventually transforms into microscopic crystalline hydroxyapatite (HAP, ideal stoichiometry = $Ca_{10}(PO_4)_6(OH)_2$).[10−12]

Macromolecules such as noncollagenous proteins are important in bone mineralization because they carry negative charges through the presence of amino acid residues, such as aspartic acid (Asp) and glutamic acid (Glu).[1] Several studies have looked into the effects of different carboxylic acid-containing additives in a calcium phosphate system.[19−27] Research in vitro on the calcium phosphate precipitation process has shown that these amino acid monomers as well as their polymeric molecules delay the phase transformation of ACP to HAP and/or control crystal growth and morphology. It has been suggested that the presence of acidic groups interacting with calcium ions through electrostatic forces dictates such events.[19−27]

The degree of polymerization of the additives also may influence the calcium phosphate precipitation reaction. Longer chain lengths carry more acidic functional groups, and possibly

Received: February 26, 2020
Revised: June 15, 2020
Published: June 29, 2020

https://dx.doi.org/10.1021/acs.jpcb.0c01690
J. Phys. Chem. B 2020, 124, 6288–6298

alter the binding energy of polymeric molecules with certain ions or surfaces. The effects of chain length of polyanions on calcium phosphate precipitation remain uncertain. Diegmueller et al. studied the effect of polyanionic molecular weight on the regulation of HAP size and shape.[27] They showed that higher molecular weight poly(Asp) (~30 kDa) and poly(Glu) (~20 kDa) have a higher affinity to HAP surfaces than lower molecular weight peptides (~10 kDa).[27] However, the specific effects of chain length on peptide−ion binding, peptide−mineral surface binding, or the calcium phosphate precipitation process could not be determined for these high molecular weight peptides (>10 kDa) due to high polydispersity that caused uncertainties in the interpretation of results.

The effects of sequences of negatively charged amino acids with low polydispersity have primarily been investigated in mineralizing calcium systems other than calcium phosphate. Hood et al. and Fischer et al. studied how oligo(Asp) and oligo(Glu) change the precipitation of calcium carbonate and calcium oxalate minerals, respectively.[28,29] It was found that the number of repeating acidic units of homooligopeptide controls the precipitation of the minerals by stabilizing certain precursor phases. We have investigated the effect of short Glu peptides on calcium phosphate mineralization in a two-part study. In the first part of this series,[30] we studied the effect of peptide concentration, i.e., variable total carboxylic acid concentration in solution. In that study, we found that longer chain oligo(Glu) delays the phase transformation of ACP to HAP.[30] Nevertheless, the mechanism by which different chain lengths of peptide alters the precursor phases and, thereby, the precipitation process has yet to be revealed.

In the present work, we systematically investigate the mechanism by which short peptide oligomers, oligo(L-glutamic acids), with a precise number of repeating units and low polydispersity affects calcium phosphate precipitation. This builds upon the accompanying work[30] by focusing on the importance of chain length versus the total amount of carboxylic acid groups in solution. Calcium phosphates were synthesized in the absence and presence of different lengths of oligo(L-glutamic acid)n (n = 3, 7, 8, and 10), each with a different peptide concentration to keep the total concentration of carboxylic groups constant. The morphology and phase of precipitates were characterized by transmission electron microscopy and X-ray scattering. Solution kinetics and calcium-oligopeptide interaction/complexation were characterized by inductively coupled plasma optical emission spectroscopy (ICP-OES), calcium ion (Ca^{2+})-selective electrode, and isothermal titration calorimetry (ITC) measurements. We show that the effects of oligo(L-glutamic acids) in calcium phosphate precipitation cannot be explained only by the total amount of carboxylic groups present in solution. The chain length, i.e., the number of acidic residues in one chain, determines the stability of ACP in vitro. Finally, we propose a mechanism for how oligopeptides with different chain lengths delay the ACP to HAP phase transformation.

2. EXPERIMENTAL METHODS

All chemicals were purchased from Sigma-Aldrich (St. Louis, MO) at the highest available purity unless otherwise specified. L-glutamic acid oligomers of different lengths were synthesized by GenScript (Piscataway, NJ) with a purity of >95%. All chemicals used in this experiment were dissolved in ultrapure deionized water with a resistivity of 18.2 MΩ·cm (Barnstead GenPure xCAD Plus, Thermo Scientific, Rockford, IL), and all solutions were filtered through a 0.1 μm membrane prior to experiments.

2.1. Crystallization Experiments. Calcium chloride ($CaCl_2$) and ammonium phosphate dibasic ($(NH_4)_2HPO_4$) were each dissolved in 10 mM HEPES buffer (pH 7.4) to make 50 mM calcium and phosphate stock solutions, respectively. Oligo(L-glutamic acid) stock solutions were prepared by dissolving each oligomer of differing chain lengths (0.5, 0.25, 0.22, and 0.18 mM peptide for the respective experimental group with Glu_3, Glu_7, Glu_8, and Glu_{10}) in HEPES buffer (10 mM, pH 7.4). In the inorganic control group, the precipitation experiment was started by diluting the calcium stock solution in HEPES buffer (10 mM, pH 7.4) to reach a concentration of 4 mM. Phosphate stock solution was then added dropwise (at a rate of ~80 $\mu L \cdot min^{-1}$) until reaching a concentration of 2.4 mM. In the peptide groups, the stock solution of peptide was first added to the diluted calcium solution followed by the dropwise addition of phosphate solution. The resulting solution was then vortexed for ~2 s and left to age for different times depending on the characterization experiment. The experiment was conducted at room temperature (25 ± 0.2 °C) with no further stirring. Different volumes of suspension were prepared for each characterization technique as explained in detail below.

2.2. Precipitate Characterization. *2.2.1. Transmission Electron Microscopy (TEM).* For the TEM experiment, 500 μL of the calcium phosphate suspension was prepared without and with peptides following the above-mentioned method. At different time points (2 min, 10 min, 30 min, 1 h, 3 h, 5 h, 8 h, and 1 d), a 7 μL aliquot was obtained from the suspension and pipetted onto a Formvar/carbon film-supported copper grid (300 mesh, Ted Pella, Inc., Redding, CA). The liquid was blotted gently with filter paper after 3 min, and the grid was allowed to air-dry overnight. Transmission electron microscopy imaging and selected area electron diffraction (SAED) were conducted on JEOL JSM-1230 (120 kV, Peabody, MA) and FEI Tecnai G2 F20 (200 kV, Hillsboro, OR), respectively. An energy dispersive X-ray spectrometer (EDS, EDAX, Mahwah, NJ) connected to the FEI Tecnai TEM was utilized to obtain the nitrogen content of the precipitates. Five different areas on each TEM grid were analyzed by EDS.

2.2.2. Dynamic Light Scattering (DLS). Dynamic light scattering experiments were conducted in situ for the first 30 min of the precipitation experiment and were started as soon as the phosphate stock solution was introduced to the calcium suspension in the absence or presence of oligo(L-glutamic acid). The total volume of the calcium phosphate suspension was 500 μL. Malvern Nano ZS Series (Malvern Panalytical, Westborough, MA) equipped with a 633 nm, 4 mW HeNe laser was used for the measurement at 173° backscatter angle at 25 °C with 11 runs of 10 s. A 5 s equilibration time was used for each measurement. The refractive indices of apatite and HEPES buffer used for data calculations were 1.630 and 1.332, respectively. The viscosity of HEPES buffer was set to be 0.8910 cP.

2.2.3. Small Angle X-ray Scattering (SAXS). Calcium phosphate suspensions at different time points (section 2.1) were centrifuged (4000 rpm, 5 min) to separate the resulting precipitate from the supernatant. The precipitate was then washed with cold water before being lyophilized to obtain dry samples that were flat-mounted between Mylar film for particle size analysis by SAXS. Intensity data were collected using a Panalytical Empyrean Nano Edition multipurpose diffractom-

https://dx.doi.org/10.1021/acs.jpcb.0c01690
J. Phys. Chem. B 2020, 124, 6288−6298

eter (Westborough, MA) equipped with a Cu source ($\lambda_{Cu\ K\alpha}$ = 0.15406 nm), a Cu focusing optic with a 1/32° fixed diffraction slit, an evacuated ScatterX78 sample stage and beam path, and a GaliPIX3D area detector.

EasySAXS (Panalytical) was used for subtraction of the measured background intensities from the sample data and desmearing based on the known instrument configuration. Two types of modeling were used for SAXS data analysis. One approach was a standard volume-weighted size distribution (Dv(R)) analysis performed using EasySAXS. A second approach used a more sophisticated "Unified" model that included both the size distribution of the particles and the structure factor from interparticle interferences.[31] In addition to scale and background, the fitted model parameters include mean size (Å) with assumed Gaussian distribution, radius of gyration (R_g, Å), power law slope (P), distance between scatterers (Å), and phi (φ), which relates to the number of nearest-neighbor scatterers. This second fitting approach was done using the Irena package for Igor Pro (v. 8.03).[32]

2.2.4. Synchrotron Total X-ray Scattering and Pair Distribution Function (PDF) Analysis. Structural information for the calcium phosphates was obtained using synchrotron total X-ray scattering and PDF analysis. Samples were loaded dry in 1 mm O.D. polyimide capillaries (Cole-Parmer, Vernon Hills, IL). The measurements were performed at an incident X-ray energy of 58.66 keV (λ = 0.2113 Å) at Sector 11 beamline ID-B of the Advanced Photon Source at Argonne National Laboratory. The scattered intensities from the samples and empty sample holder were collected using an amorphous Si 2D image detector (PerkinElmer, Waltham, MA). The geometry of the setup was calibrated from the measurement of a CeO_2 standard using Fit2D software.[33,34] The software was also used to convert the 2D image detector data into synchrotron powder XRD profiles plotted as q-space vs intensity, where $q = \frac{4\pi \sin\theta}{\lambda}$, and a 0.99 polarization correction was applied. xPDFsuite software was used for background subtraction and calculation of the PDF. The sample composition was assumed in all cases to be HAP, and the maximum q-space values used in the Fourier transformation were in the range 23−26 $Å^{-1}$.

The quantitation of the degree of phase transformation was obtained using linear combination fitting (LCF) of the real-space PDFs. The individual phase abundances were estimated using two components representing pure ACP (group with 0.18 mM Glu_{10} at 1 h) and pure HAP (inorganic control group at 3 h). The abundances were normalized to 100% and the estimated errors are approximately ±5%.

2.3. Solution Chemistry Analysis for Kinetics Study. *2.3.1. Inductively Coupled Plasma−Optical Emission Spectroscopy (ICP-OES).* Calcium and phosphate concentrations in solution over time were measured using ICP-OES. Calcium phosphate suspensions of 4 mL were prepared for this experiment. At different time points (2 min, 10 min, 30 min, 1 h, 3 h, 5 h, 8 h, 10 h, and 1 d), aliquots of 280 μL were obtained from the suspension and centrifuged at 15 000 rpm for 5 min. The supernatant with a volume of 190 μL and the resulting precipitate were then each dissolved in 5% (v/v) nitric acid solution for the measurement of Ca and P concentration using ICP-OES (ICP-OES 720, Agilent, Santa Clara, CA). The concentration of Ca and P were measured at their respective wavelengths of 396.847 and 213.618 nm, and the average of three replicates is reported.

2.3.2. Calcium Ion (Ca^{2+}) Selective Electrode. To obtain the kinetics of the calcium phosphate nucleation and growth, a Ca^{2+}-selective electrode (perfectION Combined Ion-Selective Electrode, Mettler Toledo, Columbus, OH) was utilized to track the calcium concentration in situ over a period of time. Calcium phosphate suspensions with a total volume of 5 mL were prepared in the absence or presence of oligo(L-glutamic acids), each with the addition of 100 μL of ionic strength adjustment solution (perfectION calcium ISA, Mettler Toledo). The data were obtained through a pH/ion meter (SevenCompact S220, Mettler Toledo) and recorded every 15 s (EasyDirect Software, Mettler Toledo). The calcium ion concentration at each time point was normalized to the maximum value of each measurement. The experiment was repeated three times and the average is reported.

2.3.3. Analysis of Precipitation Kinetics. The kinetics of the precipitation process were analyzed using data obtained by the Ca^{2+}-selective electrode. The data were first used to obtain the induction time (t_i), which is defined as the time at which the amorphous phase transforms into a crystalline phase and was determined from the intersection between the linear fits to two regions in the curve of the Ca^{2+} profile: a small Ca^{2+} concentration decrease and a fast Ca^{2+} concentration decrease.

The data were then used to get the rate of crystal transformation and growth, and were evaluated using a modification of the empirical "derivative method" described by Fischer et al.[29] A sixth-order polynomial fit was applied to the experimental concentration values as a function of time starting from the maximum value of each measurement:

$$c(t) = A_0 + A_1 t + A_2 t^2 + A_3 t^3 + A_4 t^4 + A_5 t^5 + A_6 t^6 \quad (1)$$

The first derivation of eq 1 was defined as the rate of desupersaturation (r):

$$r = \frac{dc(t)}{dt} = A_1 + 2A_2 t + 3A_3 t^2 + 4A_4 t^3 + 5A_5 t^4 + 6A_6 t^5 \quad (2)$$

Equating the second derivation of eq 1 to zero was used to obtain the inflection point, i.e., the time at which there is a maximum change of calcium concentration:

$$\frac{d^2 c(t)}{dt^2} = 2A_2 + 6A_3 t + 12A_4 t^2 + 20A_5 t^3 + 30A_6 t^4 = 0 \quad (3)$$

The rate when the maximum concentration change occurs (r_{max}) was then determined by substituting the t and A_i values obtained in eq 3 to the rate formula in eq 2. The retardation efficiency for each peptide was eventually calculated as

$$R = \frac{r_{control} - r_{max}}{r_{max}} \quad (4)$$

in which $r_{control}$ corresponds to the maximum rate of the control group and r_{max} corresponds to that of each peptide group.

2.4. Binding between Oligopeptide and Calcium Ions. *2.4.1. Ca^{2+}-Selective Electrode.* First 10 mL of 0.4 mM calcium solution was prepared in HEPES buffer (10 mM, pH 7.4). Subsequently, 500 μL of 5 mM peptide stock solution (in 10 mM HEPES, pH 7.4) was pipetted into the calcium solution. The free Ca^{2+} in the solution ($[Ca^{2+}]_p$) after peptide addition was measured using a pH/ion meter (SevenCompact S220, Mettler Toledo) equipped with a perfectION Combined

https://dx.doi.org/10.1021/acs.jpcb.0c01690
J. Phys. Chem. B 2020, 124, 6288−6298

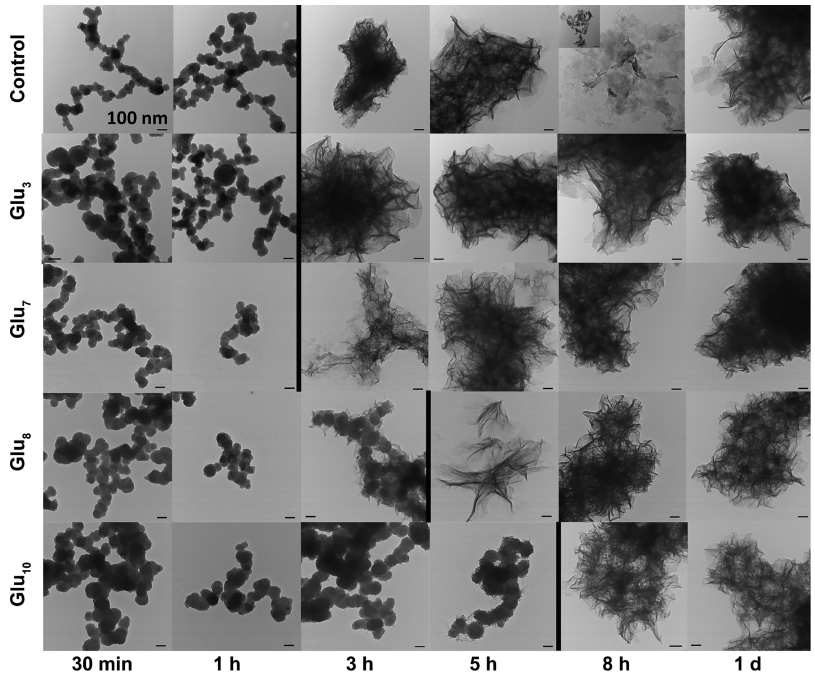

Figure 1. TEM images of different morphologies during calcium phosphate precipitation over time in the absence or presence of 2 mM carboxylic concentration using different chain length oligo(L-glutamic acids). The vertical black lines denote the times at which the transformation from the spherical chain-like structures to a ribbon-like morphology occurs.

Ion-Selective Electrode (Mettler Toledo) in voltage mode (mV). The free Ca^{2+} in the absence of peptide ($[Ca^{2+}]_f$) was determined by measuring the voltage of 10 mL calcium solution (0.4 mM) after an addition of 500 μL of 10 mM HEPES buffer solution. Two hundred μL of ionic strength adjustment solution (~40% (w/w) KCl in water, perfectION calcium ISA, Mettler Toledo) was also added to the calcium solutions without or with peptide (ionic strength: ~0.1 M). Four potential difference measurements at 0, 5, 15, and 30 min were collected in each group over the course of 30 min. Both $[Ca^{2+}]_p$ and $[Ca^{2+}]_f$ values were calculated using a calibration curve, which was determined by measuring potential difference at different known concentrations of calcium.

The concentration of bound Ca^{2+} ($[Ca^{2+}]_b$) was calculated according to

$$[Ca^{2+}]_b = [Ca^{2+}]_f - [Ca^{2+}]_p \quad (5)$$

The number (n') of bound Ca^{2+} ions per deprotonated peptide (L^{y-}) can then be determined using the equation:

$$n' = \frac{[Ca^{2+}]_b}{[L^{y-}]} \quad (6)$$

However, it was not practically possible to determine $[L^{y-}]$ accurately. Therefore, we defined the number of Ca^{2+} bound per peptide as

$$n = \frac{[Ca^{2+}]_b}{[\text{peptide}]} \quad (7)$$

The trend of n with peptide length is expected to be the same as that of n' as a greater charge per peptide is expected as the chain length increases.

2.4.2. Isothermal Titration Calorimetry (ITC). To obtain information on the binding constant of each peptide with calcium ions, ITC experiments were conducted. The ITC instrument (NANO ITC, TA Instrument, New Castle, DE) used in this study was equipped with a 1 mL sample cell and an identical reference cell with adiabatic shield in a vacuum-tight chamber. Each peptide solution (overfilled) with a volume of 1 mL was injected into the sample cell and the reference cell was loaded with 1 mL of 10 mM HEPES solution. The calcium solution was loaded into a 250 μL titration syringe. The sample cell was stirred at 300 rpm throughout the experiment and the temperature in the cell was kept constant at 25 °C. Each 10 μL injection took 15 s and the time between each injection was set to be 600 s. The heat rate data were subtracted to the background data before the peak area was integrated for data analysis using NanoAnalyze software (TA Instrument). The n values for each peptide were fixed using those obtained in section 2.4.1 by eq 7. The ITC data provide the effective association constants ($K_{a,eff}$) between Ca^{2+} and each peptide that take into account sequential reactions, including the deprotonation of the peptide and binding of Ca^{2+} and the peptide (eq 8).

$$nCa^{2+} + H_yL \rightleftharpoons (Ca_nH_{y-m}L)^{(2n-m)+} + mH^+ \quad (8)$$

3. RESULTS AND DISCUSSION

3.1. Morphological and Phase Evolution during the Precipitation Process. *3.1.1. TEM Analysis.* Calcium phosphate precipitation was conducted at room temperature without or with the addition of oligo(L-glutamic acids) at peptide concentrations of 0.5, 0.25, 0.22, and 0.18 mM for Glu_3, Glu_7, Glu_8, and Glu_{10}, respectively, to reach the total carboxylic group concentration of 2 mM for each peptide. The morphological features of the precipitates obtained over time are shown in Figure 1. In all groups between 2 min and 1 h of the reaction, the precipitation process results in the formation of interconnected spherical particles (50−100 nm) to form a chain-like structure. The chains of spherical particles are

https://dx.doi.org/10.1021/acs.jpcb.0c01690
J. Phys. Chem. B 2020, 124, 6288−6298

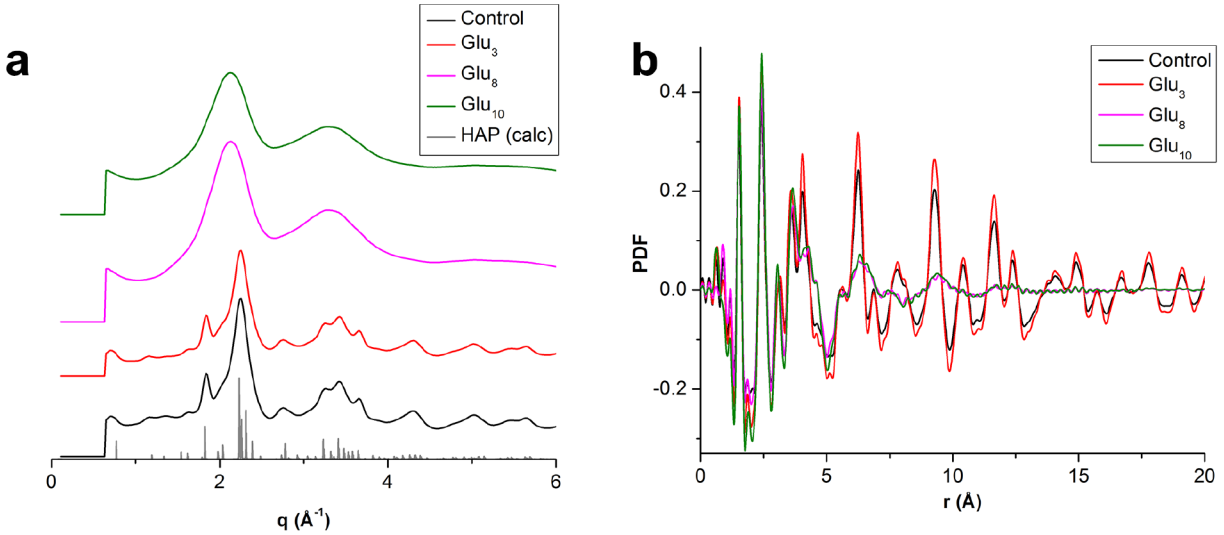

Figure 2. Synchrotron pXRD (a) and PDF (b) profiles of precipitates at 3 h without or with oligo(L-glutamic acids) at the same concentration (2 mM) of carboxylic acid group.

composed of ACP as shown by in the representative SAED patterns of the Glu_3 and Glu_{10} samples at 1 h (Figures S1a and S2a). The SAED patterns show no evidence of diffraction rings, suggesting an amorphous phase. This chain-like structure, which is the typical morphology of ACP, has also been shown in previous studies on calcium phosphate precipitation.[6,16,25,35] The amorphous precursors are known to be comprised of 10−20 wt % of tightly bound water.[10]

Over time, a new distinct morphology is observed in all groups, where a ribbon-like structure forms. The transformation from the chain-like to the ribbon-like structure, however, occurs at different time points depending on the peptide chain length. Groups with Glu_3 and Glu_7 transform by 3 h, similar to the control system, and Glu_8 by 5 h and Glu_{10} by 8 h. This morphology is characteristic of the appearance of a new calcium phosphate phase, synthetic crystalline apatite.[6,16] The crystallinity of the phase is evident from electron diffraction patterns (Figures S1b and S2b) that are consistent with HAP (112) and (002) faces, as shown for the Glu_3 and Glu_{10} systems at their respective phase transformation times, 3 and 8 h. The formation of this structure is preceded by the appearance of spikes on the surface of the spherical particles in the chain-like structure. These spikes can be observed clearly for the Glu_8 group at 3 h and the Glu_{10} group at 5 h (Figure 1), suggesting that the ACP serves as the nucleation template for the new HAP crystalline phase. These TEM results suggest that despite having the same total amount of carboxylic groups in solution, the stabilization of ACP and the delay of the phase transformation to HAP depend on the chain length of oligo(L-glutamic acids). The longest peptide, Glu_{10}, carrying 11 carboxylic groups per chain shows the most stabilization compared to the shorter peptides.

3.1.2. Calcium Phosphate Phase Determination by Scattering Experiments. The local and intermediate-range order of the precipitates was characterized by X-ray scattering methods. Figure 2a shows the synchrotron powder X-ray diffraction (pXRD) patterns obtained for control, Glu_3, Glu_8, and Glu_{10} at 3 h. Two distinct patterns are observed: relatively strong and well-defined peaks for the control and Glu_3 groups and diffuse and overlapping peaks for the Glu_8 and Glu_{10} groups. The presence of the sharp peaks in the control and Glu_3 suggest that the precipitates contain a more crystalline phase by 3 h. Although broadened, the observed peaks correlate well with the calculated HAP reference peaks (Figure 2a, gray), confirming that the observed crystalline phase by TEM and SAED is HAP. Precipitates obtained in the presence of Glu_8 and Glu_{10}, however, appear to remain amorphous at 3 h, correlating well to the TEM and SAED results above. The PDF profiles from high energy SAXS are also consistent with these results (Figure 2b) by showing that Glu_8 and Glu_{10} have structural order only to ∼12 Å, which is consistent with an amorphous phase. In comparison, Glu_3 and the control show peaks in the PDF to 20 Å and beyond, suggesting crystalline HAP with longer-range structural order. The evolution of the precipitate phase by synchrotron pXRD is shown in Figure S3 for each peptide group.

Pair distribution function (PDF) profiles (Figure S4) were obtained to determine if the peptide length affects the local order in the ACP. Results show similar local structure in all groups, as discussed in the accompanying study.[30] The PDF profiles at different time points in each peptide group are shown in Figure S4. The PDF profiles obtained were further analyzed using LCF to estimate ACP and HAP phase abundances at different time points (Table 1). Within an hour of precipitation, precipitates are mostly present as ACP, but there is a minor presence of HAP, except in the group with Glu_{10}. The control and Glu_3 precipitates transform from ACP to HAP almost completely by 3 h (94% and 98% HAP, respectively). The group with Glu_8 transforms to a similar extent (>90%) only at 5 h, while transformation of Glu_{10} does not near completion until 8 h.

3.2. Solution Chemistry Analysis and Precipitation Kinetics. *3.2.1. ICP-OES.* The change in calcium and phosphate solution concentrations during the precipitation reaction was determined ex situ using ICP-OES. Parts a and b of Figure 3 show the Ca and P concentrations at each time point, respectively, relative to each initial concentration. There is an initial drop of Ca and P concentrations in all groups in the first 2 min, where 80% of the bulk Ca and P concentrations remain in the solution. This drop is related to the formation of ACP. The same extent of Ca and P depletion is seen for all groups, indicating that the peptides apparently do not affect

https://dx.doi.org/10.1021/acs.jpcb.0c01690
J. Phys. Chem. B 2020, 124, 6288−6298

Table 1. Estimation of Phase Abundances by LCF at Different Time Points in the Absence or Presence of Oligo(L-glutamic acids) with a Constant Total Amount of Carboxylic Acid Groups (2 mM) in Solution

group	time (h)	ACP (%)	HAP (%)
control	1	95	5
control	3	6	94
Glu_3	1	85	15
Glu_3	3	2	98
Glu_8	1	96	4
Glu_8	3	93	7
Glu_8	5	7	93
Glu_8	8	7	93
Glu_{10}	1	100	0
Glu_{10}	3	94	6
Glu_{10}	5	20	80
Glu_{10}	8	8	92

the initial ACP nucleation. The concentrations then remain constant up to 1 h for all groups. As the reaction continues, in the control and Glu_3 groups, a second decrease occurs between 1 and 3 h, while a similar change is detected in the Glu_7 group between 1 and 5 h before the curve reaches a plateau. The second decrease in Ca and P concentrations in Glu_8 and Glu_{10} occurs even later in the reaction, between 3 and 5 h and 5−8 h, respectively. The current results correspond well to the morphological evolution observed by TEM (Figure 1). Thus, the second decrease in concentration is attributed to uptake of Ca and P from solution into the ACP. The homopeptide with the most repeating units, the decamer, shows the greatest delay in the uptake of calcium and phosphate from the solution to the growing precipitates. These data further support the result that different chain lengths of peptide affect calcium phosphate precipitation differently in spite of having the same total concentration of acidic carboxylic group in solution.

3.2.2. Ca^{2+}-Selective Electrode. The progress of the reaction in situ was observed using Ca^{2+}-selective electrode. Figure 3c shows that Glu_{10} delays the decrease of Ca^{2+} concentration the most (up to 3 h) compared to other peptides. Groups with Glu_3, Glu_7, and Glu_8 do not show much difference in the time of the Ca^{2+} drop. However, the time when the curve reaches a plateau in the Glu_8 group is much later compared to control and groups with shorter peptide length. The results by Ca^{2+}-selective electrode, which allow continuous monitoring in situ, tend to show an earlier concentration drop compared to TEM and ICP-OES experiments. Despite not precisely matching the time points

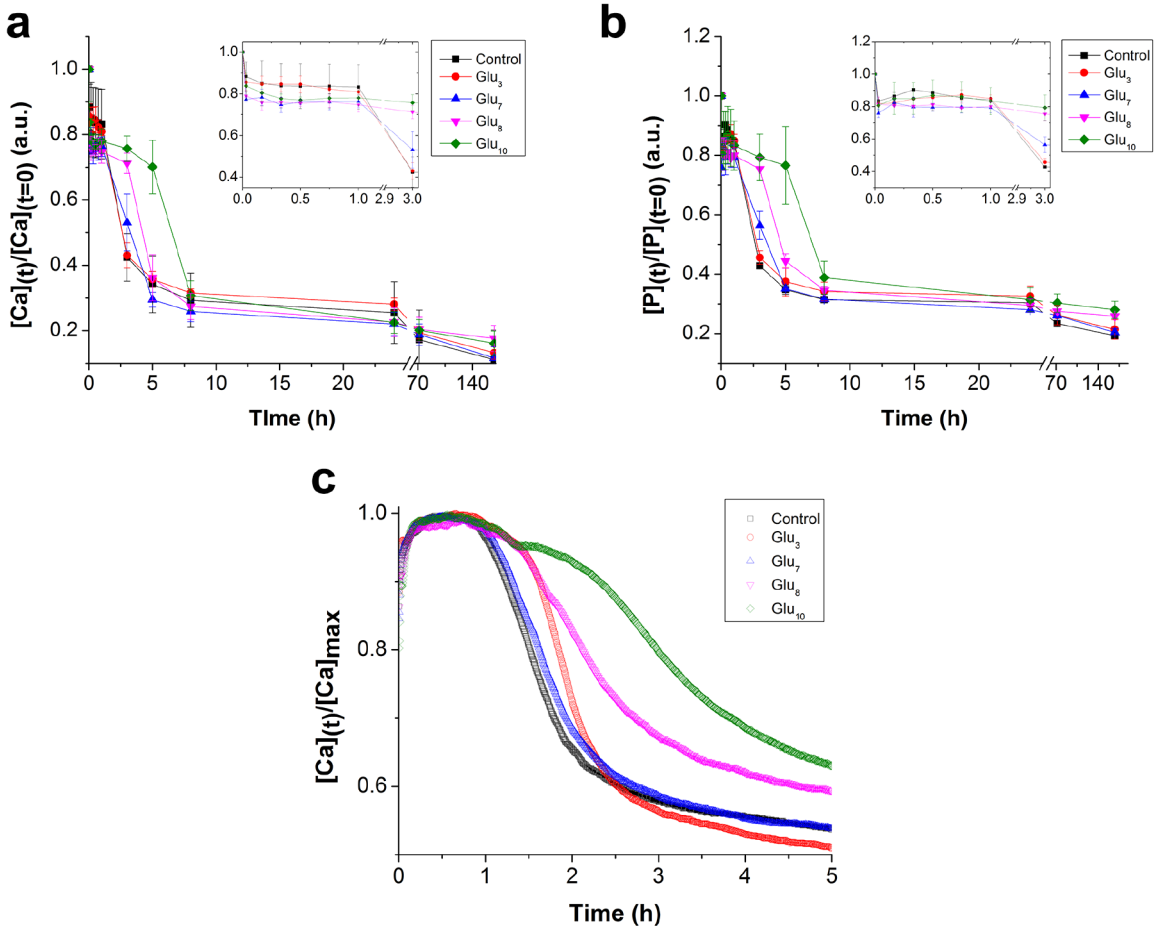

Figure 3. Solution analysis during calcium phosphate precipitation. The progress of relative calcium (a) and phosphate (b) concentrations in the supernatant normalized by each initial concentration obtained by ICP-OES. Error bars are standard error from the average of three different experiments. Relative Ca^{2+} concentration (c) normalized by the maximum value obtained using a Ca^{2+}-selective electrode in a solution containing both calcium and phosphate.

https://dx.doi.org/10.1021/acs.jpcb.0c01690
J. Phys. Chem. B 2020, 124, 6288−6298

obtained ex situ by TEM and ICP-OES, the Ca^{2+}-selective electrode data show a similar trend dependent on peptide chain length.

3.2.3. Kinetics Analysis. The data obtained by Ca^{2+}-selective electrode were also analyzed to obtain the kinetics of precipitation. Table 2 contains the induction time (t_i) at which the ACP first transforms to crystalline HAP, the maximum rate of transformation and growth of the crystalline HAP phase (r_{max}), and the calculated retardation efficiency (R) of each peptide. The t_i values do not show an overall trend. Nonetheless, the Glu_{10} group shows a value almost double compared to the other groups, suggesting that HAP nucleation with this peptide is inhibited the most.

Table 2. Calculated Induction Time (t_i), Rate of Crystal Transformation and Growth (r_{max}), and Retardation Efficiency (R) for Each Peptide Obtained by Analysis of in Situ Ca^{2+}-Selective Electrode Data[a]

group	t_i (h)	r_{max} (h^{-1})	R
control	1.132 ± 0.156	0.367 ± 0.057	n/a
Glu_3	1.483 ± 0.011	0.341 ± 0.009	0.071 ± 0.024
Glu_7	1.051 ± 0.043	0.309 ± 0.015	0.159 ± 0.040
Glu_8	1.219 ± 0.120	0.208 ± 0.031	0.435 ± 0.083
Glu_{10}	2.130 ± 0.121	0.151 ± 0.009	0.589 ± 0.023

[a]Standard error was obtained from the average of three separate experiments.

The r_{max} and R values (Table 2) obtained through our kinetics experiments provide quantitative information about the peptide chain length effect on calcium phosphate precipitation. The r_{max} values decrease consistently from control to Glu_{10} whereas the R values increase consistently. The group with the shortest peptide chain length, Glu_3, has a value of r_{max} that is very similar to the control and is less than 1% effective in retarding phase transformation, indicating that the addition of the short peptide does not influence the phase transformation process. The heptamer is able to slow down the phase transformation by 16%, and the octamer is able to further delay the transformation by up to 44% compared to the control group. The decamer shows a retardation efficiency close to 60%, the most compared to other peptide groups. A similar trend was also observed in a previous study on calcium oxalate system with different lengths of glutamic acid peptide and a constant concentration of carboxylic groups.[29] The present kinetics results further confirm that the chain length of the peptide modulates calcium phosphate precipitation at a constant concentration of carboxylic acid groups.

3.2.4. Peptide–Ca^{2+} Binding Interaction. Here, the binding interaction between each peptide with Ca^{2+} was determined by Ca^{2+}-selective electrode and ITC. The free Ca^{2+} concentration in the solution decreases as the peptide chain length increases; i.e., the amount of Ca^{2+} bound to each peptide increases as chain length increases (Figure 4). The $K_{a,eff}$ shows that the overall binding reactions become stronger as the chain length increases (Table 3; Figure S5). Thus, the longer oligopeptides bind more calcium ions per peptide (n) and the $K_{a,eff}$ is larger than for the shorter peptides. These two results are important in explaining that each oligopeptide is associated with the calcium ions differently, thus, delaying the phase transformation at different time points. The mechanism for the delayed phase transformation will be discussed below.

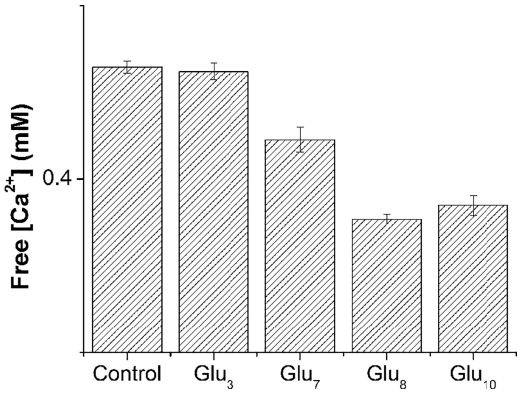

Figure 4. Free Ca^{2+} concentration upon introduction of oligo(L-glutamic acids) to Ca^{2+} solution (no phosphate present) displaying peptide–Ca^{2+} interaction. The error bars represent the standard error from the average of three separate experiments.

Table 3. Thermodynamic Parameters in the Binding between Ca^{2+} and Oligo(L-glutamic acids) from ITC Measurement Using an Independent Model[a]

group	n	$K_{a,\,eff}$ (M^{-1})	ΔH (kJ·mol^{-1})	ΔS (J·mol^{-1}·K^{-1})
Glu_3	0.16	3.00×10^2	35.37	166.1
Glu_7	0.24	1.87×10^3	5.38	80.66
Glu_8	0.34	1.84×10^3	7.97	89.24
Glu_{10}	0.32	2.12×10^3	12.96	107.1

[a]Values obtained from eq 7 in section 2.4.1

3.3. ACP Size Evolution and ACP–Peptide Association. Particle size distributions of the ACP precipitates were determined by SAXS and Dv(R) analysis, and also by DLS. The association of the amorphous precursors with the peptides was determined by EDS.

3.3.1. Primary Particle Size by SAXS. The background-subtracted SAXS profiles for the ACP formed with and without peptides generally display two types of behavior. For the control and Glu_3 samples, the curves are approximately linear at low q and become increasingly asymptotic at $q > 1.1$ nm^{-1} (Figure 5a). For the Glu_8 and Glu_{10} samples, a region of increased intensity develops at $q > 0.9$ nm^{-1}. The fit to the SAXS data is shown in Figure S6. A volume-weighted size distribution (Dv(R)) analysis of the SAXS intensities shows the average radii of the primary particles in each sample (Figure 5b) and the control. Table 4 summarizes the fit results using both Dv(R) and unified model. Overall, the average mean radii of the particles from the two modeling approaches are practically identical. The analyses show that all of the precipitates at 1 h are extremely small with a diameter of less than 1.5 nm. The data show that particles in the control system and with the shortest peptide, Glu_3, are smaller compared to those with longer peptides. These ~1–1.5 nm-sized primary particles aggregate to form the secondary spherical particles of size 50–100 nm observed by TEM and DLS, and the secondary particles further form tertiary aggregates as detected by DLS. It is noteworthy that the average size estimated by SAXS for the control and Glu_3 samples may be affected by the onset of crystallization due to the presence of the (100) reflection for hydroxylapatite, which has a d-spacing of approximately 8 Å. We expect the effect to be small because HAP is relatively minor in abundance (≤6%); however, it is

https://dx.doi.org/10.1021/acs.jpcb.0c01690
J. Phys. Chem. B 2020, 124, 6288–6298

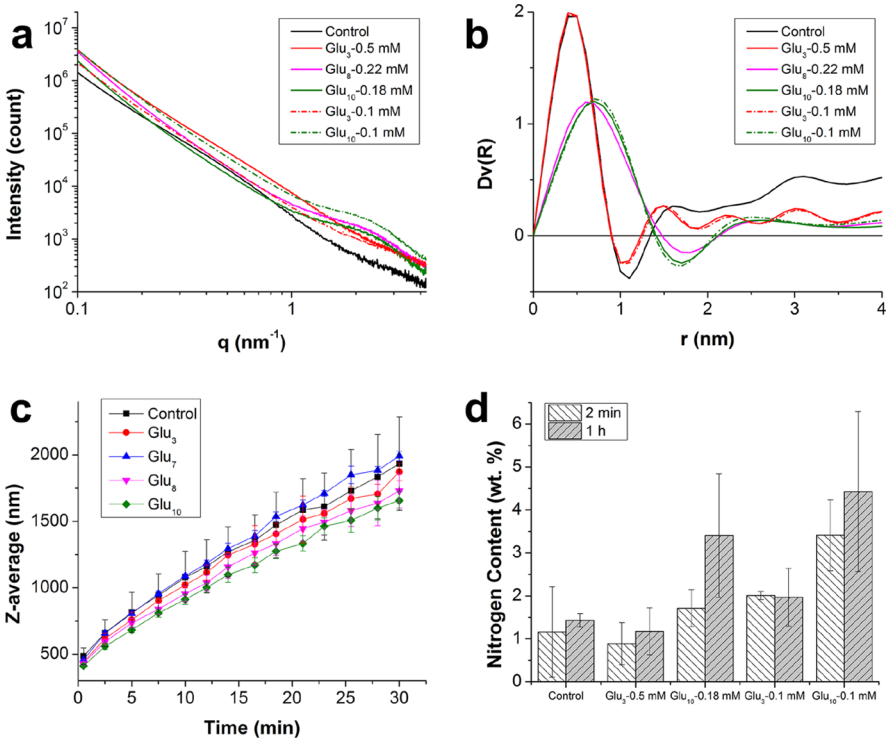

Figure 5. ACP particle size evolution and ACP-peptide association. Background-subtracted SAXS data (a) and radii of the precipitates obtained at 1 h using Dv(R) analysis (b). Diameter of secondary particles and tertiary aggregates measured by DLS in the first 30 min of precipitation without or with oligo(L-glutamic acids) (c). Nitrogen content of the precipitates at 2 min and 1 h obtained by EDS (d). Error bars show standard error from the average of three separate experiments (c) and of five different areas on the TEM grid (d).

Table 4. Dv(R) Fit Results for the Samples Precipitated With and Without Oligo(L-glutamic acids) at 1 h

		0.1 mM peptide		2 mM total COOH		
	control	Glu_3	Glu_{10}	Glu_3	Glu_8	Glu_{10}
most freq radius (nm)[a]	0.50	0.40	0.71	0.50	0.60	0.70
average radius (nm)[a]	0.45	0.44	0.70	0.47	0.69	0.70
average radius (nm)[b]	0.61	0.64	0.90	0.40	0.91	0.94
R20 (nm)[a]	0.28	0.28	0.44	0.29	0.41	0.43
R50 (nm)[a]	0.45	0.45	0.71	0.47	0.68	0.70
R80 (nm)[a]	0.61	0.61	0.97	0.65	0.96	0.98
relative std dev (%)[a]	38.15	38.24	39.68	39.29	42.86	40.94
power law (P)[b]	3.17	2.74	2.84	2.62	2.87	2.83
distance (nm)[b]	0.76	0.76	2.42	0.76	2.52	2.3
φ[b]	1.37	1.14	1.09	1.35	0.68	0.94

[a]Obtained using Dv(R) analysis. [b]Obtained using "Unified" model.

not possible to separate the effect in the current analysis and will be the focus of future work.

Fitting the SAXS profiles with the unified model confirms the primary particle sizes and also reveals differences in the distances between the centers of neighboring particles. In the case of the control and Glu_3, the distances between the particle are approximately equal to twice the radius, which indicates that the particles are effectively touching one another. In the case of Glu_8 and Glu_{10}, the distances between the particle centers range from 23 to 25 Å. Given the particle radii are approximately 9 Å, this indicates that the particles are not in contact and are separated by distances of 5−7 Å. The increased distance between particles precipitated in the presence of longer chain lengths correlates with a decrease in phi (φ), which indicates relatively fewer nearest neighbor particles. Some other similarities and differences are also noted. The power law (P) values suggest that all of the samples have fractal dimensions with rough interfaces.[36]

3.3.2. Aggregate Size by DLS. Dynamic light scattering measurements allow us to track the aggregate size development as the precipitation proceeds in the absence or presence of oligo(L-glutamic acids). Figure 5c shows that within 30 s of reaction, there is a formation of secondary particles with a diameter of 250−500 nm. Relatively smaller-sized aggregates are produced in the presence of Glu_{10}. As the precipitation continues, the particle size grows larger to form tertiary aggregates in all groups, but Glu_{10} maintains the smallest aggregate size consistently up to 30 min.

3.3.3. Peptide Association with ACP Particles. Figure 5d depicts the nitrogen content of ACP particles obtained by EDS on the control, Glu_3, and Glu_{10} groups at 2 min and 1 h at different concentrations of peptide in solutions as noted on the x-axis. These EDS data show an association of peptides with the ACP particles. Particles with Glu_{10} contain more nitrogen compared to those in control and Glu_3 samples. This is consistent with Glu_{10} having longer amino acid sequences. However, the nitrogen data are not able to reveal the location of the associated peptides with respect to the particles (on the surface or in the particles).

The SAXS results show larger primary particle sizes in the presence of longer oligopeptides. If there is association of peptides within the precipitated amorphous particles (occlusion), then the larger peptide will result in larger primary particle sizes. The effect of peptide chain length on the primary

https://dx.doi.org/10.1021/acs.jpcb.0c01690
J. Phys. Chem. B 2020, 124, 6288−6298

particle size excludes the possibility that peptides are associated only on the surface of the particle. In the latter case, the particles formed in the presence of peptide would all have the same size as the control group or a smaller size than the control, if the adsorption of peptide decreases interfacial energy. However, the latter effect, if present, seems to be less important than the effect of occlusion for determining the primary particle size.

In the submicrometer to micrometer length scale measured by DLS, the particles formed in the presence of longer chain length show smaller aggregate size compared to the control group. Thus, the present DLS results suggest that association of the peptides with the secondary particles and tertiary aggregates occurs on the surface as well, resulting in a reduced ACP−water interfacial energy and, thereby, a smaller aggregate size.

3.4. Proposed Mechanism. The results of our various analytical methods may be summarized as follows. The formation of ACP is rapid, and the kinetics of ACP formation are not influenced by oligopeptide chain length. The local order of the ACP is also not influenced by the peptide length. However, the primary particle size is affected with larger primary particles being formed in the presence of longer peptides. The primary particles aggregate into secondary spherical particles and chain-like tertiary structures. The longer peptides bind more Ca^{2+} and bind with the Ca^{2+} more strongly. Peptides are occluded within the primary particles, which affects primary particle size, and are associated with the surface of secondary and tertiary aggregates which influences their aggregation. Longer peptides reduce interfacial energy to a greater extent, resulting in smaller secondary and tertiary aggregates than shorter peptides and the control. The ACP aggregates transform into crystalline HAP over time. The peptide length influences the time at which transformation occurs with longer peptides delaying the transformation to a greater extent than shorter peptides, which is also confirmed by kinetics data analysis. These results are synthesized in detail below, and a mechanism is proposed to explain peptide chain length effect on delaying ACP to HAP phase transformation.

The mechanism by which ACP transforms to HAP in the presence of oligo(L-glutamic acid)$_n$ starts with the association of calcium ions and peptide in the solution (Figure 6). Upon the addition of phosphate stock solution, the ACP nuclei are rapidly formed and the oligo(L-glutamic acid)$_n$ is occluded within the precipitates. These precursors are stable for a period of time before the HAP nuclei are formed. The growth of this crystalline phase decreases the concentration of calcium and phosphate from the solution rapidly.

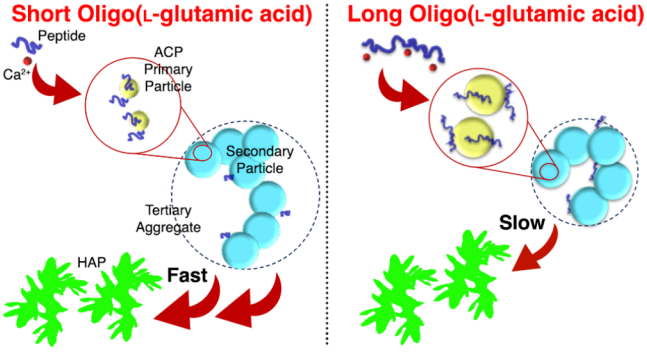

Figure 6. Schematic of proposed mechanism for the delayed phase transformation of ACP to HAP.

In detail, during the first 2 min upon the introduction of phosphate stock solutions into the calcium solution without or with oligo(L-glutamic acids), amorphous precipitates are observed. Despite being associated with the precipitates as reflected in the EDS results (Figure 5d), the presence of any length of peptides does not discernably affect the time at which the ACP nucleates (Figures 1−3). However, the association of the longer peptide increases the size of the amorphous primary particles that are formed as seen in our SAXS results (parts a and b of Figure 5 and Table 4; Figure 6).

Our results show that ACP is stable for a long period of time compared to its formation rate in all groups, as there is no change in calcium and phosphate concentrations in the solution for at least 1 h (Figure 3). This indicates that there might be a steady state between the uptake of ions from the solution and the formation of ACP. The plateau in calcium and phosphate concentrations with time is not limited to the experimental peptide groups but is also observed in the inorganic control group.

The ACP precursors then phase transform to HAP at different time points depending on the chain length of oligo(L-glutamic acids) for a certain concentration of acidic carboxylic groups in the bulk solutions (Figure 6). The long plateau in concentrations of Ca and P after the formation of ACP followed by a sharp decrease in concentrations also suggests that the formation of HAP nuclei is the rate-determining step in the formation of calcium phosphate crystalline phase. Our findings reveal that the longer the homooligomer is, the more stable is the ACP; i.e., it takes longer to nucleate HAP, and the crystal growth process is slower (Table 2). Additionally, the longer peptides with delayed phase transformation have larger primary particle sizes compared to the shorter peptides, as well as a larger distance between primary particles as seen in SAXS data (parts a and b of Figure 5 and Table 4; Figure 6). Having fewer neighboring particles in the presence of longer peptide could delay the transformation if the fusion of aggregating particles is required for phase transformation. It is, however, unclear by which mechanism the ACP particles transform into HAP nuclei, i.e., whether it is through a dissolution-reprecipitation mechanism or through solid-to-solid phase transformation and whether or not this increased spacing delays phase transformation.[6,37,38]

The mechanism by which the different chain length homopeptides affect the phase transformation is proposed to arise through its occlusion within the ACP precipitates, as concluded from the SAXS data. An earlier study suggests that the increase in the phase transformation rate in the presence of high molecular weight peptides is associated with the lowering of the interfacial energy of HAP nuclei by adsorbed peptides.[6] However, neither in their study nor in ours is the HAP−water interfacial energy in the presence of peptide actually measured. In our case, the association of longer peptide chains results in smaller secondary and tertiary aggregate size (Figure 5c) but delayed phase transformation, suggesting that ACP−water interfacial energy might be reduced by the longer peptide.

In addition to lowering the ACP−water interfacial energy, peptide occlusion within the ACP primary particles provides an alternative/additional explanation for the delayed phase transformation. Occluded peptide associated with Ca^{2+} (Figure 4 and Table 3) in the amorphous particles presumably influences the rate at which ACP transforms to HAP (Figure 3

https://dx.doi.org/10.1021/acs.jpcb.0c01690
J. Phys. Chem. B 2020, 124, 6288−6298

and Table 2). During transformation, crystal rearrangement, removal of water, and uptake of calcium occur.[10,12,22,39] In the presence of peptides, rearrangement can only occur when the associated peptides are removed from the lattices to form an ordered structure. The more calcium ions that are bound to the peptide, and the stronger the binding is, the more difficult it is to rearrange the ions. We have shown that the longer peptides bind more Ca^{2+} per peptide and also bind the ions more strongly (Figure 4 and Table 3). The presence of the peptides within the amorphous precursors will also affect the rate at which water is removed, which is needed for the phase transformation to occur. The longer peptide tends to be more hydrophilic than the shorter ones, thus attracting more water molecules, and this association will presumably prolong the dehydration process.

4. CONCLUSIONS

Following upon our previous work,[30] the current study investigates if the total amount of carboxylic acid groups present in the system solely controls calcium phosphate precipitation. This was facilitated by using short oligo(L-glutamic acids) with well-controlled molecular weight and polydispersity. We find that the chain length, i.e., the number of contiguous acidic groups a peptide carries, is an important factor during the precipitation reaction at a given concentration of carboxylic acid groups. Furthermore, we propose a mechanism for the delayed phase transformation of ACP to HAP in the presence of peptides. The longer chain length stabilizes the amorphous phase by having more bound calcium ions per peptide and this binding is stronger to the longer peptides compared to the shorter peptides. One possible mechanism is that this association reduces the ACP−water interfacial energy, thus stabilizing ACP phase and delaying phase transformation of ACP to HAP. Another mechanism might be through the occlusion of peptide within the ACP particles, thus extending the time needed for ACP to rearrange its structure and to dehydrate in order to transform into crystalline calcium phosphates. This work expands our understanding of specific interactions between organic additives, especially those bearing a contiguous amino acid sequence, and minerals. Additionally, this information provides information on control over the mineralization process for the improved design of biomimetic mineralized materials using short-chain peptides.

■ ASSOCIATED CONTENT

Supporting Information

The Supporting Information is available free of charge at https://pubs.acs.org/doi/10.1021/acs.jpcb.0c01690.

SAED patterns, synchrotron pXRD and PDF ITC thermograms, and SAXS data fit (PDF)

■ AUTHOR INFORMATION

Corresponding Author

Nita Sahai − *Department of Polymer Science, Department of Geosciences, and Integrated Bioscience Program, The University of Akron, Akron, Ohio 44325, United States;* orcid.org/0000-0003-3852-0557; Email: sahai@uakron.edu

Authors

Putu Ustriyana − *Department of Polymer Science, The University of Akron, Akron, Ohio 44325, United States;* orcid.org/0000-0001-9804-3081

F. Marc Michel − *Department of Geosciences, Virginia Polytechnic Institute and State University, Blacksburg, Virginia 24061, United States*

Michael C. Wilson − *Department of Polymer Science, The University of Akron, Akron, Ohio 44325, United States*

Emma Harmon − *Department of Polymer Science, The University of Akron, Akron, Ohio 44325, United States*

Jiahui Chen − *Department of Polymer Science, The University of Akron, Akron, Ohio 44325, United States;* orcid.org/0000-0002-3861-146X

Tianbo Liu − *Department of Polymer Science, The University of Akron, Akron, Ohio 44325, United States;* orcid.org/0000-0002-8181-1790

Complete contact information is available at: https://pubs.acs.org/10.1021/acs.jpcb.0c01690

Notes

The authors declare no competing financial interest.

■ ACKNOWLEDGMENTS

We greatly acknowledge technical support on scattering experiments provided by the Virginia Tech National Center for Earth and Environmental Nanotechnology Infrastructure (NanoEarth) staff at Virginia Tech and the Virginia Tech Crystallography Lab (VTX). We are grateful for the technical assistance on SAED provided by Dr. Min Gao at the Advanced Materials and Liquid Crystal Institute, Kent State University, Kent, OH. We appreciate the invaluable discussion on acid−base interactions of polyacids with Drs. Abdala Bashir and Derek Luong. We acknowledge financial support provided by start-up funds from The University of Akron and generous gift funds from Dr. Edward Weil to N.S.; The Robert Helm Jr. Fellowship in Polymers and Biomaterials awarded to PU; and Lubrizol for a Biomimicry Fellowship to M.C.W. F.M.M. gratefully acknowledges support provided by the National Science Foundation (NSF) through CAREER-1652237. This research used resources of the Advanced Photon Source, a US Department of Energy (DOE) Office of Science User Facility, operated for the DOE Office of Science by Argonne National Laboratory under Contract No. DE-AC02-06CH11357. Beamtime for the data collection presented in this paper was allocated under GUP 64554. This work was also supported by NanoEarth, a member of the National Nanotechnology Coordinated Infrastructure (NNCI), supported by NSF (ECCS 1542100). T.L. acknowledges support from NSF (CHE1904397).

■ REFERENCES

(1) George, A.; Veis, A. Phosphorylated Proteins and Control over Apatite Nucleation, Crystal Growth, and Inhibition. *Chem. Rev.* **2008**, *108*, 4670−4693.

(2) Boskey, A.; Maresca, M.; Ullrich, W.; Doty, S.; Butler, W.; Prince, C. Osteopontin-Hydroxyapatite Interactions in Vitro: Inhibition of Hydroxyapatite Formation and Growth in a Gelatin-Gel. *Bone Miner.* **1993**, *22*, 147−159.

(3) de Bruyn, J. R.; Goiko, M.; Mozaffari, M.; Bator, D.; Dauphinee, R. L.; Liao, Y.; Flemming, R. L.; Bramble, M. S.; Hunter, G. K.; Goldberg, H. A. Dynamic Light Scattering Study of Inhibition of

Nucleation and Growth of Hydroxyapatite Crystals by Osteopontin. *PLoS One* **2013**, *8*, No. e56764.
(4) He, G.; Dahl, T.; Veis, A.; George, A. Nucleation of Apatite Crystals in Vitro by Self-Assembled Dentin Matrix Protein 1. *Nat. Mater.* **2003**, *2*, 552−8.
(5) He, G.; Gajjeraman, S.; Schultz, D.; Cookson, D.; Qin, C.; Butler, W. T.; Hao, J.; George, A. Spatially and Temporally Controlled Biomineralization Is Facilitated by Interaction between Self-Assembled Dentin Matrix Protein 1 and Calcium Phosphate Nuclei in Solution. *Biochemistry* **2005**, *44*, 16140−8.
(6) Tsuji, T.; Onuma, K.; Yamamoto, A.; Iijima, M.; Shiba, K. Direct Transformation from Amorphous to Crystalline Calcium Phosphate Facilitated by Motif-Programmed Artificial Proteins. *Proc. Natl. Acad. Sci. U. S. A.* **2008**, *105*, 16866−70.
(7) Hunter, G. K.; Goldberg, H. A. Nucleation of Hydroxyapatite by Bone Sialoprotein. *Proc. Natl. Acad. Sci. U. S. A.* **1993**, *90*, 8562−5.
(8) Hunter, G. K.; Goldberg, H. A. Modulation of Crystal Formation by Bone Phosphoproteins: Role of Glutamic Acid-Rich Sequences in the Nucleation of Hydroxyapatite by Bone Sialoprotein. *Biochem. J.* **1994**, *302* (1), 175−9.
(9) Yang, Y.; Cui, Q.; Sahai, N. How Does Bone Sialoprotein Promote the Nucleation of Hydroxyapatite? A Molecular Dynamics Study Using Model Peptides of Different Conformations. *Langmuir* **2010**, *26*, 9848−59.
(10) Wang, L.; Nancollas, G. H. Calcium Orthophosphates: Crystallization and Dissolution. *Chem. Rev.* **2008**, *108*, 4628−69.
(11) Wang, L.; Nancollas, G. H. Pathways to Biomineralization and Biodemineralization of Calcium Phosphates: The Thermodynamic and Kinetic Controls. *Dalton Trans* **2009**, 2665−72.
(12) Sikiric, M. D.; Furedi-Milhofer, H. The Influence of Surface Active Molecules on the Crystallization of Biominerals in Solution. *Adv. Colloid Interface Sci.* **2006**, *128*−*130*, 135−58.
(13) Mahamid, J.; Aichmayer, B.; Shimoni, E.; Ziblat, R.; Li, C.; Siegel, S.; Paris, O.; Fratzl, P.; Weiner, S.; Addadi, L. Mapping Amorphous Calcium Phosphate Transformation into Crystalline Mineral from the Cell to the Bone in Zebrafish Fin Rays. *Proc. Natl. Acad. Sci. U. S. A.* **2010**, *107*, 6316−6321.
(14) Mahamid, J.; Sharir, A.; Addadi, L.; Weiner, S. Amorphous Calcium Phosphate is a Major Component of the Forming Fin Bones of Zebrafish: Indications for an Amorphous Precursor Phase. *Proc. Natl. Acad. Sci. U. S. A.* **2008**, *105*, 12748−53.
(15) Nudelman, F.; Pieterse, K.; George, A.; Bomans, P. H.; Friedrich, H.; Brylka, L. J.; Hilbers, P. A.; de With, G.; Sommerdijk, N. A. The Role of Collagen in Bone Apatite Formation in the Presence of Hydroxyapatite Nucleation Inhibitors. *Nat. Mater.* **2010**, *9*, 1004−9.
(16) Habraken, W. J.; Tao, J.; Brylka, L. J.; Friedrich, H.; Bertinetti, L.; Schenk, A. S.; Verch, A.; Dmitrovic, V.; Bomans, P. H.; Frederik, P. M.; et al. Ion-Association Complexes Unite Classical and Non-Classical Theories for the Biomimetic Nucleation of Calcium Phosphate. *Nat. Commun.* **2013**, *4*, 1507.
(17) Posner, A. S.; Betts, F. Synthetic Amorphous Calcium Phosphate and Its Relation to Bone Mineral Structure. *Acc. Chem. Res.* **1975**, *8*, 273−281.
(18) Tropp, J.; Blumenthal, N. C.; Waugh, J. S. Phosphorus Nmr Study of Solid Amorphous Calcium Phosphate. *J. Am. Chem. Soc.* **1983**, *105*, 22−26.
(19) Burke, E. M.; Guo, Y.; Colon, L.; Rahima, M.; Veis, A.; Nancollas, G. H. Influence of Polyaspartic Acid and Phosphophoryn on Octacalcium Phosphate Growth Kinetics. *Colloids Surf., B* **2000**, *17*, 49−57.
(20) Cantaert, B.; Beniash, E.; Meldrum, F. C. The Role of Poly(Aspartic Acid) in the Precipitation of Calcium Phosphate in Confinement. *J. Mater. Chem. B* **2013**, *1*, 6586.
(21) Wang, Z.; Xu, Z.; Zhao, W.; Sahai, N. A Potential Mechanism for Amino Acid-Controlled Crystal Growth of Hydroxyapatite. *J. Mater. Chem. B* **2015**, *3*, 9157−9167.
(22) Bar-Yosef Ofir, P.; Govrin-Lippman, R.; Garti, N.; Füredi-Milhofer, H. The Influence of Polyelectrolytes on the Formation and Phase Transformation of Amorphous Calcium Phosphate. *Cryst. Growth Des.* **2004**, *4*, 177−183.
(23) Jahromi, M. T.; Yao, G.; Cerruti, M. The Importance of Amino Acid Interactions in the Crystallization of Hydroxyapatite. *J. R. Soc., Interface* **2013**, *10*, 20120906.
(24) Tavafoghi Jahromi, M.; Cerruti, M. Amino Acid/Ion Aggregate Formation and Their Role in Hydroxyapatite Precipitation. *Cryst. Growth Des.* **2015**, *15*, 1096−1104.
(25) Jiang, S.; Pan, H.; Chen, Y.; Xu, X.; Tang, R. Amorphous Calcium Phosphate Phase-Mediated Crystal Nucleation Kinetics and Pathway. *Faraday Discuss.* **2015**, *179*, 451−61.
(26) Hentrich, D.; Junginger, M.; Bruns, M.; Börner, H. G.; Brandt, J.; Brezesinski, G.; Taubert, A. Interface-Controlled Calcium Phosphate Mineralization: Effect of Oligo(Aspartic Acid)-Rich Interfaces. *CrystEngComm* **2015**, *17*, 6901−6913.
(27) Diegmueller, J. J.; Cheng, X.; Akkus, O. Modulation of Hydroxyapatite Nanocrystal Size and Shape by Polyelectrolytic Peptides. *Cryst. Growth Des.* **2009**, *9*, 5220−5226.
(28) Hood, M. A.; Landfester, K.; Muñoz-Espí, R. The Role of Residue Acidity on the Stabilization of Vaterite by Amino Acids and Oligopeptides. *Cryst. Growth Des.* **2014**, *14*, 1077−1085.
(29) Fischer, V.; Landfester, K.; Muñoz-Espí, R. Stabilization of Calcium Oxalate Metastable Phases by Oligo(L-Glutamic Acid): Effect of Peptide Chain Length. *Cryst. Growth Des.* **2011**, *11*, 1880−1890.
(30) Ustriyana, P.; Harmon, E.; Chen, K.; Michel, F. M.; Sahai, N. Oligo(L-Glutamic Acids) in Calcium Phosphate Precipitation: Chain Length Effect. *J. Phys. Chem. B* **2020**, DOI: 10.1021/acs.jpcb.0c01689.
(31) Beaucage, G. Approximations Leading to a Unified Exponential/Power-Law Approach to Small-Angle Scattering. *J. Appl. Crystallogr.* **1995**, *28*, 717−728.
(32) Ilavsky, J.; Jemian, P. R. Irena: Tool Suite for Modeling and Analysis of Small-Angle Scattering. *J. Appl. Crystallogr.* **2009**, *42*, 347−353.
(33) Hammersley, A. *Fit2d: An Introduction and Overview*; European Synchrotron Radiation Facility: Grenoble, France, 1997.
(34) Hammersley, A. P.; Svensson, S. O.; Thompson, A. Calibration and Correction of Spatial Distortions in 2d Detector Systems. *Nucl. Instrum. Methods Phys. Res., Sect. A* **1994**, *346*, 312−321.
(35) Jiang, S.; Jin, W.; Wang, Y.-N.; Pan, H.; Sun, Z.; Tang, R. Effect of the Aggregation State of Amorphous Calcium Phosphate on Hydroxyapatite Nucleation Kinetics. *RSC Adv.* **2017**, *7*, 25497−25503.
(36) Schmidt, P. W. A Review of Some Recent Applications of Small-Angle Scattering in Studies of Polydisperse Systems and Porous Materials. *Makromol. Chem., Macromol. Symp.* **1988**, *15*, 153−166.
(37) Boskey, A. L.; Posner, A. S. Conversion of Amorphous Calcium Phosphate to Microcrystalline Hydroxyapatite. A Ph-Dependent, Solution-Mediated, Solid-Solid Conversion. *J. Phys. Chem.* **1973**, *77*, 2313−2317.
(38) Lotsari, A.; Rajasekharan, A. K.; Halvarsson, M.; Andersson, M. Transformation of Amorphous Calcium Phosphate to Bone-Like Apatite. *Nat. Commun.* **2018**, *9*, 4170.
(39) Brečević, L.; Hlady, V.; Füredi-Milhofer, H. Influence of Gelatin on the Precipitation of Amorphous Calcium Phosphate. *Colloids Surf.* **1987**, *28*, 301−313.

https://dx.doi.org/10.1021/acs.jpcb.0c01690
J. Phys. Chem. B 2020, 124, 6288−6298